Title

An Improved Understanding of the Natural Resonances of Moonpools contained within Floating Rigid-Bodies: Theory and Application to Oscillating Water Column Devices

Corresponding Author

Diana Bull

Sandia National Laboratories

P.O. Box 5800 MS 1124

Albuquerque, NM 87185-1124

(1) 505 284 5607

Abstract

The fundamental interactions between waves, a floating rigid-body, and a moonpool that is selectively open to atmosphere or enclosed to purposefully induce pressure fluctuations are investigated. The moonpool hydrodynamic characteristics and the hydrodynamic coupling to the rigid-body are derived implicitly through reciprocity relations on an array of field points. By modeling the free surface of the moonpool in this manner, an explicit hydrodynamic coupling term is included in the equations of motion. This coupling results in the migration of the moonpool's natural resonance frequency from the piston frequency to a new frequency when enclosed in a floating rigid-body. Two geometries that highlight distinct aspects of marine vessels and oscillating water column (OWC) renewable energy devices are analyzed to reveal the coupled natural resonance migration. The power performance of these two OWCs in regular waves is also investigated. The air chamber is enclosed and a three-dimensional, linear, frequency domain performance model that links the rigid-body to the moonpool through a linear resistive control strategy is detailed. An analytic expression for the optimal linear resistive control values in regular waves is presented.

Keywords

Moonpool, natural resonance, wave energy converter, oscillating water column, resistive damping control, BBDB

1. Introduction

The dynamics of a floating rigid-body that contains an opening to the free surface of the water within the submerged volume of the rigid-body, i.e. a moonpool, must consider both the wave-activation of the rigid-body itself, the wave-activation of the moonpool, and the coupled activation between the rigid-body and moonpool. There are two main classes of moonpools considered in this paper: those that are open to the atmosphere above the internal free surface and those with an enclosed air chamber, vented to the atmosphere through a power generation turbine, above the moonpool. Open moonpools are often found in marine vessels that are used for drilling applications or research; the marine vessels with moonpools considered here are those designs with the internal waterline equivalent to the external waterline. Moonpools with an enclosed air chamber are a class of wave energy converter (WEC) called Oscillating Water Column (OWC) devices. As the incident waves cause pressure fluctuations in the air chamber of an OWC, the spinning turbine will produce power. For the OWC the relative motion between the rigid-body and the internal free surface that produces pressure fluctuations is enhanced in order to generate power, whereas for marine vessels this relative motion should be minimized.

Accurate modeling of floating OWCs and marine vessels with moonpools requires that both the wave-activated rigid-body and the wave-activated internal water column be modeled in a hydrodynamically coupled fashion. Hydrodynamic coupling is required as each are activated by incoming waves and the motion of either the rigid-body or the internal water column is able to reciprocally activate motions in the other. To date, much work has been devoted to understanding the natural resonances of a moonpool in a rigid-body that is not activated by waves, i.e. a fixed rigid-body. The piston resonance (ω_{piston}) is the primary hydrodynamically uncoupled resonance. By simplifying the

water column as a mass-spring system such that resonance occurs when the mass of the internal water column times the acceleration is equal to the hydrostatic restoring force, Faltinsen (O.M. Faltinsen, 1990) derived an analytical expression to illustrate the effect of the moonpool draft on its natural frequency. Molin (Molin, 2001) derived analytic relationships for the moonpool natural frequencies and associated shapes of the free surface using the geometric parameters describing the moonpool contained within a fixed rigid-body.

However, there are limited studies that investigate how a floating rigid-body affects the moonpool resonance. There have been quite a few experimental studies of floating rigid-bodies with moonpools (Wei et al., 2011)(Maisondieu and Le Boulluec, 2001) (Maisondieu and Ferrant, 2003)(Yang and Kwon, 2013). Some of these studies (Maisondieu and Ferrant, 2003) (Yang and Kwon, 2013) explicitly acknowledge the experimental moonpool natural resonance when contained within a floating rigid-body is not located at the theoretical ω_{piston}. The other studies are more focused on deriving relationships between the geometric properties of the moonpool and the location of the theoretical ω_{piston}. These studies are not able to analytically describe how the floating rigid-body affects the moonpool in large part because the methodology used to model the wave – rigid-body – moonpool interactions have not used modeling techniques that explicitly employ the hydrodynamic coupling terms between the rigid-body and the moonpool.

Modeling of a rigid-body activated by waves is well understood and fully developed. The potential flow boundary value problem used to predict small-amplitude floating rigid-body motions assumes irrotational flow of an incompressible and inviscid fluid. The free-surface and rigid-body-boundary value conditions are then linearized and resolved within Boundary Element Method (BEM) solvers by individually solving for the incident, diffracted, and radiated velocity potentials on a series of panels constituting the 3-dimensional wetted surface. The wave-activated floating rigid-body dynamics

can be directly obtained using any one of the commercially or academically available linear potential flow BEM solvers, like WAMIT (*WAMIT*, n.d.).

Modeling of the internal water column is not as developed as that for the floating rigid-body. There are two approaches to modeling the internal free surface: as a rigid weightless piston (Evans, 1978) or through calculation of the pressure distribution (Evans, 1982) (Sarmento and Falcão, 1985). The first approach is only valid for small internal free surface areas and is akin to a 2-body treatment in which the oscillating rigid-body and the moonpool are treated independently. The second approach does not place limitations on the size of the internal free surface area and utilizes a BEM solver to model the dynamics of the moonpool. Calculation of the internal pressure distribution at the surface of the moonpool can be accomplished in three ways: approximated, solved for explicitly, or solved for implicitly (Lee et al., 1996) (Lee and Nielson, 1996). Approximation utilizes the technique of generalized modes (Lee et al., 1996) which expands upon the rigid piston approximation to include additional modes in other degrees of freedom (corresponding to standing waves inside the moonpool) (*WAMIT*, n.d.). Explicit calculation requires determination of the velocity potential for the internal free surface. This is currently possible in WAMIT v7.0; however, the implicit calculation will result in exactly the same analytic expressions and is possible with most potential flow BEM solvers. Implicit calculation utilizes reciprocity relations to solve for all of the internal free surface hydrodynamic parameters from the oscillating rigid-body's potential using an array of field points on the internal free surface. Implicit calculation, presented in (Lee and Nielson, 1996) and (Falnes, 2002) and applied by (Kurniawan et al., 2011) and (Bull and Johnson, 2013), is pursued in this paper allowing for the use of standard potential flow BEM solvers, such as WAMIT v6.4 (*WAMIT*, n.d.).

The effect of hydrodynamically coupling a floating rigid-body to a moonpool is seen explicitly when the equations of motion for the coupled system are developed such that the rigid-body and the internal water column are coupled with a hydrodynamic parameter. This paper will analytically show

how the floating rigid-body affects the moonpool's natural resonance by explicitly including the hydrodynamic coupling between the rigid-body and the moonpool—i.e. this paper will show that ω_{piston} is not the location for the natural resonance of the moonpool in a hydrodynamically coupled system. This effect is pronounced for asymmetric rigid-bodies and moonpools with large areas, aspects that are common in a certain types of OWCs.

Two rigid-body profiles were selected to highlight two extremes of the effect of the rigid-body hydrodynamic properties on the moonpool natural resonance: the surface area of the moonpool and the symmetry characteristics of the rigid-body. The first device is the Backward Bent Duct Buoy (BBDB) (Masuda et al., 1987) which mimics the asymmetries seen in marine vessels with a plane of symmetry along the elongated hull. This device has a large moonpool with an entrained water mass that is seven times the displaced mass. Further, the asymmetric profile results in cross-coupling between the heave-pitch and the heave-surge rigid-body modes, thus further contributing to the influence on the moonpool natural resonance location. The second device is an axisymmetric point absorber design resembling an upside down glass with the moonpool centerline coincident with that of the rigid-body's ('Model A' studied by Alves (Alves, 2012)). This device has a small moonpool with an entrained water mass that is only thirty percent of the displaced mass. Further, there is no cross-coupling in the rigid-body modes that can contribute to the coupling term between the rigid-body and the moonpool.

This paper will be divided into two main sections; the first section, Section A, will consider only the wave – rigid-body – moonpool interaction problem and will highlight the analytic expressions that illustrate the floating rigid-body's effect on the moonpool resonance location. The effect will be investigated on the two rigid-body profiles discussed above by comparing their hydrodynamically coupled volume flow responses against their respective uncoupled volume flow responses.

The second section, Section B, will focus on expanding this wave – rigid-body – moonpool interaction problem to include a power conversion chain (PCC) capable of absorbing power from the

waves. The performance model for a floating OWC links the rigid-body to the pressure oscillations above the moonpool through a control strategy implemented with a representation of the PCC. The PCC representation used here is a simple linear relationship between pressure and flow, proportional to a resistive damping value. By explicitly formulating the hydrodynamic equations of motion to include the coupling between the rigid-body and the moonpool, the optimal form of purely resistive control is shown to incorporate this coupling. This analytic expression is applied and the resulting dynamics and power absorption characteristics are compared for the two device profiles in regular waves.

2. Rigid-Body Geometries

The dynamics of a floating rigid-body are dependent upon both the below-water profile and the structural properties. Hence the rigid-bodies are modeled both in MultiSurf (*MultiSurf*, n.d.) for input into the BEM solver to determine the hydrodynamic parameters discussed above, and in SolidWorks (*SolidWorks 3D CAD Design Software*, n.d.) to determine the mass distribution. The structural designs assume uniform thickness of A36 steel, appropriate ballast mass and placement, and an estimate of the mass and location of the PCC. An average wall thickness of 35.1 mm is applied to the entirety of both devices. However, this structural design likely has a much larger factor of safety than is needed on most parts of the rigid-body and hence should not be considered optimized. The ballast is distributed to obtain the desired draft and ensure that the center of gravity and the center of buoyancy are aligned vertically. The mass of the PCC (drivetrain, generator, power conditioning electronics) is approximated from the results presented in (Smith et al., 2014) and is placed at the expected center of the PCC location.

Neither of the geometries have been optimized. Optimization of the geometry could entail selecting water column length and surface area to maximize the irregular wave performance in a deployment climate (Falcão et al., 2012) (Gomes et al., 2012) (Wei et al., 2011). Optimization could also

target viscous losses or encourage weathervaning as is depicted in industrial designs (Ocean Energy Ltd., n.d.).

The global and body coordinate systems adopted for the hydrodynamic models are identified in Fig. 1 A and Fig. 2 A. The global coordinate system is identified in blue and is at the undisturbed water level directly above the body coordinate system in both Fig. 1 A and Fig. 2 A. The incident wave velocity potential φ_o, and hence the phases of the exciting forces, are defined relative to the global coordinate system. The rigid-body panels shown in Fig. 1 B and Fig. 2 B are defined relative to the center of gravity (COG), which defines the location of the body coordinate system identified in gold in in both Fig. 1 A and Fig. 2 A. The body forces and motions calculated by WAMIT are calculated relative to this coordinate system.

Panels representing the 3-dimensional wetted surface of the floating OWC are used by the BEM potential flow solver. Fig. 1 B and Fig. 2 B illustrate the discretization of panels as well as identify the BEM calculation methodology through color. The panel density increases towards corners by applying cosine spacing to the discretization. Green panels indicate that the velocity potential is obtained from the wave source potential; cyan panels indicates that velocity potential is obtained without calculation of the source potential; and grey panels indicate the area of irregular frequency removal. The panels are analyzed in WAMIT using the higher-order method.

2.1 BBDB

The BBDB design is L-shaped with the opening to the ocean downstream from the wave propagation direction. This device was extensively studied for the US Department of Energy sponsored Reference Model Project("Reference Model Project. Sandia National Laboratories.," n.d.) (Bull et al., 2014). Fig. 1 A illustrates the structural design of the BBDB, while Fig. 1 B shows the hydrodynamic counterpart (note only the wetted surface must be modeled for the potential flow BEM solver). The width of the device is 27 m. The majority of the device dimensions were selected based upon the

conclusions of the following papers (Imai et al., 2011),(Suzuki et al., 2011), and (Hong et al., 2004). The ballast is assumed to be seawater and is added to the buoyancy chambers as shown in Fig. 1 A (yellow areas labeled Bow and Stern).

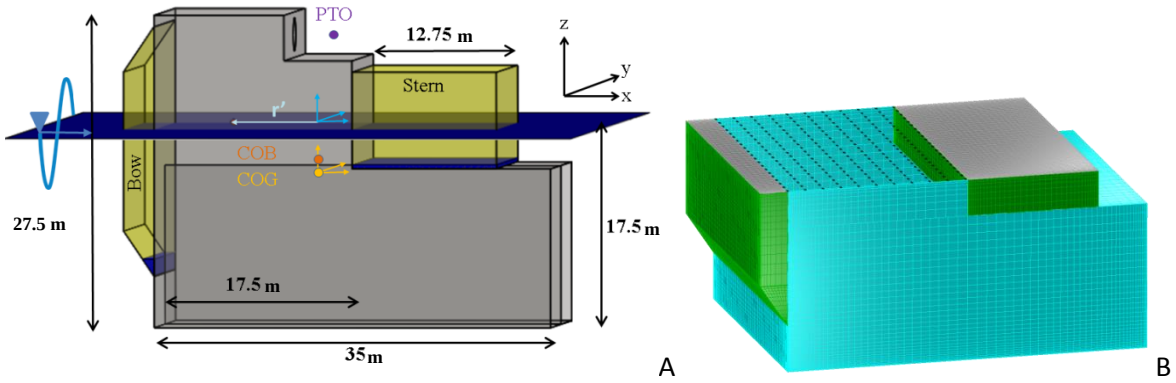

Fig. 1. A) Model of the BBDB describing dimensions in m, locations of principal components, locations of the COB and COG, and identifying coordinate systems B) Wetted surface geometry modeled in MultiSurf. Black points illustrate the interior field point locations.

TABLE I summarizes the structural properties of the device that are needed as input into WAMIT (*WAMIT*, n.d.).

Displaced Mass [kg]		2,024,657		
Structural Mass [kg]		1,808,944		
Bow Ballast Mass [kg]		22,072		
Stern Ballast Mass [kg]		123,641		
Power Conversion Mass [kg]		70,000		
Submerged Surface Area [m^2]		4,251		
COG (x,y,z) [m]		0.00	0.00	-4.29
COB (x,y,z) [m]		0.00	0.00	-3.31
Free Surface Center (x,y,z) [m]		-5.12	0.00	0.00
Radius of Gyration at COG	x	12.53	0.00	3.35
	y	0.00	14.33	0.00
	z	3.35	0.00	14.54

TABLE I. Structural properties of the asymmetric floating BBDB OWC.

An array of 231 field points describing the interior free surface of the BBDB is defined with respect to the global coordinate system. This array is illustrated in Fig. 1 B with black points. The field points capture the dynamic pressure and velocity distributions of the free surface. Due to the device plane of symmetry at $y = 0$, only half of the device is modeled in (*WAMIT*, n.d.).

2.2 Axisymmetric

Fig. 2 A illustrates the structural design of the axisymmetric device, while Fig. 2 B shows the hydrodynamic counterpart. The ballast is assumed to be concrete in order to avoid metacentric stability concerns and is added to the buoyancy chamber as shown in Fig. 2 A.

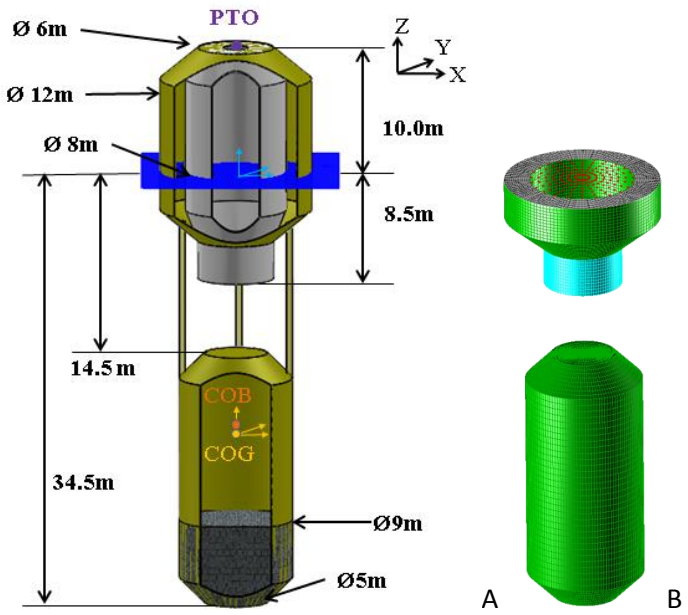

Fig. 2. A) Model of the axisymmetric OWC describing dimensions in m, locations of principal components, locations of the COB and COG, and identifying coordinate systems. B) Wetted surface geometry modeled in MultiSurf. Red points illustrate the interior field point locations.

TABLE II summarizes the structural properties of the device that are needed as input into WAMIT (*WAMIT*, n.d.).

Displaced Mass [kg]		1,468,388		
Structural Mass [kg]		493,338		
Ballast Mass [kg]		897,118		
Power Conversion Mass [kg]		70,000		
Submerged Surface Area [m^2]		1,092		
COG (x,y,z) [m]		0.00	0.00	-21.01
COB (x,y,z) [m]		0.00	0.00	-20.49
Free Surface Center (x,y,z) [m]		0.00	0.00	0.00
Radius of Gyration at COG	x	15.42	0.00	0.00
	y	0.00	15.42	0.00
	z	0.00	0.00	3.59

TABLE II. Structural properties of the axisymmetric floating OWC

Alves (Alves, 2012) employed the method of generalized modes for his hydrodynamic model, and hence did not utilize field points to describe the interior free surface of the OWC, as illustrated in Fig. 2 B with the array of 175 red points. As with the BBDB, the field points capture the dynamic pressure

and velocity distributions on the free surface and allow for an implicit calculation of the hydrodynamic parameters relating to the free surface. The axisymmetric nature of the device requires only one quarter of the device to be modeled in WAMIT (*WAMIT*, n.d.).

2.3 Comparison

The scale of these two devices is dissimilar; the displaced mass of the BBDB is 27% larger than that of the axisymmetric design, and the mass of water entrained in the BBDB water column is ~7 times more than the displaced mass while it is approximately 30% of the displaced mass of the axisymmetric device. Further the natural resonance of the OWC is dependent upon the length and free surface area of the water column (Wei et al., 2011) and, as will be described more fully in Sec. A.2.4, also on the coupling between the wave-activated rigid-body and internal water column. A comparison of key differences between the two devices is given in Table III.

	BBDB	Axisymmetric
Equilibrium Entrained Water Mass [kg]	15,255,844	437,938
Length of Water Column [m]	35	8.5
Surface Area of Water Column [m^2]	473	50
Heave Natural Period [sec]	16.1	10.7
Pitch Natural Period [sec]	11.6	37.0
Coupled OWC Natural Period [sec]	8.61	7.46

Table III Comparison of key differing properties of the two floating OWCs.

Section A.

A.1. Hydrodynamic Formulation of a Floating Rigid-body with a Moonpool

For any floating rigid-body with a moonpool both the rigid-body and the moonpool will react to the incident wave field. The reaction can be determined by employing linear potential flow theory, in which the total velocity potential is composed of the incident and diffracted potentials as well as the rigid-body and internal free surface radiation potentials. The general equation for the velocity potential of i moving bodies oscillating in all rigid-body modes j with k internal free surfaces is given by:

$$\hat{\phi} = \hat{\phi}_o + \hat{\phi}_d + \sum_{ij} \varphi_{ij} \hat{u}_{ij} + \sum_{k} \varphi_k \hat{p}_k \qquad 1$$

following the notation of (Falnes, 2002). The hat, $\widehat{\ }$, indicates complex amplitudes, $\hat{\phi}_o$ is the incident potential, $\hat{\phi}_d$ is the diffracted potential, $\sum_{ij} \varphi_{ij} \hat{u}_{ij}$ are the bodies' radiation potentials where $\hat{u}_i$ is the oscillation velocity of the i^{th} rigid-body, and $\sum_k \varphi_k \hat{p}_k$ are the internal free surface radiation potentials where $\hat{p}_k$ is the dynamic pressure fluctuation. Given this general formalism, there will be two coupled hydrodynamic equations describing the wave – rigid-body – moonpool interactions: one will capture the total force acting on the rigid-body and the other the total volume flow resulting from the internal free surface oscillations. Each of these equations will be composed of the superposition of the hydrodynamic parameters (excitation, radiation, and coupling), which are the solution to the linear potential theory formalism. The hydrodynamic coupling term acknowledges that an oscillating rigid-body will result in internal free surface oscillations of the moonpool and reciprocally that oscillations of the moonpool will result in rigid-body oscillations.

The following sections explore the governing equations for each state of the air chamber—either open to atmosphere or enclosed. This treatment will clearly highlight the effect that hydrodynamic coupling plays on the dynamic response of the rigid-body and free surface to incident waves.

A.1.1 Governing Equations for a Floating Rigid-body with an Enclosed Moonpool

The total hydrodynamic force, F_{TH}, acting on the j^{th} mode of the rigid-body is given by the combination of the excitation parameter f_j found by holding the body fixed in that direction ($u_j = 0$) scaled by the incident wave amplitude A, the radiated force $\sum_{j'} Z_{jj'} u_{j'}$ with $Z_{jj'}$found by unit-oscillation velocity $u_{j'}$of the body with the air chamber vented to atmosphere ($p = 0$), and hydrodynamic coupling parameter H_j^p that accounts for unit-fluctuation of the air-pressure p inducing rigid-body oscillations:

$$F_{TH,j} = f_j A - \sum_{j'} Z_{jj'} u_{j'} - H_j^p p \qquad j = 1, \dots, 6. \tag{2}$$

In Eq. 2, $Z_{jj'}$ is the radiation impedance of the j^{th} mode due to unit-oscillation in one of the six j' rigid body modes. Note that the angular frequency (ω) dependent complex amplitudes and sinusoidal time-dependence ($e^{i\omega t}$ with time given by t) are assumed for the hydrodynamic (f_j, $Z_{jj'}$, and H_j^p) and state ($u_{j'}$ and p) parameters.

The total hydrodynamic volume flow, Q_{TH}, resulting from oscillation of the internal free surface is given by the excitation volume flow parameter q found by venting the air-chamber to atmosphere ($p = 0$) scaled by A, the radiated volume flow Yp with Y found by unit-fluctuation of the pressure p in the enclosed air-chamber without allowing the body to oscillate ($u_j = 0$), and hydrodynamic coupling parameter H_j^u that accounts for unit-oscillation velocities u_j inducing hydrodynamic volume flow:

$$Q_{TH} = qA - Yp - \sum_j H_j^u u_j. \qquad 3$$

In Eq. 3, Y is the radiation admittance of the free surface, and is analogous to the radiation impedance of the oscillating rigid-body.

The introduction of the hydrodynamic coupling parameters (H_j^p, H_j^u) in Eq.'s 2 and 3 will result in a shifting of the expected resonances for each of the systems (oscillating rigid-body and oscillating moonpool). The magnitude of the hydrodynamic coupling in comparison to the magnitude of the other terms will determine the influence of the hydrodynamic coupling on the rigid-body's and moonpool's natural resonance frequencies.

A.1.2 Governing Equations for a Floating Rigid-body with an Open Moonpool

When considering the governing equations for a moonpool open to atmosphere, it is clear that there can be no pressure fluctuations, but a volume flow remains because the internal free surface can still oscillate. Setting the terms with a pressure p in them to zero in Eq.'s 2 and 3 above, the total hydrodynamic force is now given by:

$$F_{TH,j} = f_j A - \sum_{j'} Z_{jj'} u_{j'} \qquad j = 1, \dots, 6. \tag{4}$$

It is clear from Eq. 4 that the structural natural resonances are the same as a hydrodynamically uncoupled design when the air chamber is open to atmosphere. This indicates that the natural resonance frequencies of the rigid-body cannot be altered by a moonpool open to atmosphere.

The total hydrodynamic volume flow is now given by:

$$Q_{TH} = qA - \sum_{j} H_j^u u_j. \tag{5}$$

Contrary to the structural response, Eq. 5 shows that the oscillating water column is affected by the hydrodynamic coupling even when the air chamber is open to atmosphere. Each rigid-body mode has the potential to affect the total hydrodynamic flow. Thus, the effect on the total hydrodynamic flow and the coupled water column's resonance frequencies is influenced by both the magnitude of the coupling term (driven by the total surface area) and the number of rigid-body modes through which coupling occurs.

A.1.3 Moonpool Hydrodynamic Parameters

The frequency and directionally dependent hydrodynamic parameters in Eq. 2 and 4 relating to the floating rigid-body are given as standard output from WAMIT (*WAMIT*, n.d.) and are not discussed further. Detailed below is the determination of each of the hydrodynamic parameters identified in Eq. 3 and 5 through implicit calculation employing an array of field points.

The hydrodynamic terms relating to the internal free surface are found utilizing a combination of the oscillating body's radiation potential on an array of field points defining the internal free surface, reciprocity relations, and mathematical equivalence. The formalism presented below to obtain the internal water column hydrodynamic parameters follows Falnes (Falnes, 2002)

The excitation volume flow is found through

$$q(\omega) = \frac{1}{A}\iint_S \frac{\partial(\phi_o + \phi_d)}{\partial z} dS \quad (6)$$

where A is the incident wave amplitude, the integral is taken over the internal free surface S, ϕ_o is the incident wave velocity potential, and ϕ_d is the diffracted wave velocity potential. This integration is computed discretely by obtaining the excitation vertical velocities, $\frac{\partial(\phi_o+\phi_d)}{\partial z}$, at each field point. Note that this formulation of the problem only accounts for heave excitation.

The radiation admittance is obtained explicitly through

$$Y(\omega) = -\iint_S \frac{\partial \varphi}{\partial z} dS = G + iB \quad (7)$$

where φ is the internal free surface radiation potential, $G = \text{Re}\{Y\}$ is the radiation conductance, and $B = \text{Im}\{Y\}$ is the radiation susceptance of the internal free surface. However, the solution for the radiation admittance does not require the explicit form of φ. As presented in (Evans, 1982), the radiation conductance is related to the excitation volume flow through the following reciprocity relationship

$$G(\omega) = \frac{2k}{8\pi\rho g v_g}\int_0^{\pi} |q(\beta)|^2 \, d\beta \quad (8)$$

where the integration from 0 to π already acknowledges the transverse symmetry of the rigid-bodies, q is the excitation volume flow found in Eq. 6, β defines the incident wave-headings, k is the wave-number, ρ is the density of water, g is gravity, and v_g is the group velocity. Since the radiation admittance is causal, the radiation susceptance can be found from the radiation conductance through the Kramers-Kronig relationship

$$B(\omega) = -\frac{2\omega}{\pi}\int_0^{\infty} \frac{G(y)}{y^2 - \omega^2} dy \quad (9)$$

where the integral is to be understood in the principal value sense and is most readily evaluated with a Hilbert Transformation. The numerator $G(y)$ is the radiation conductance from Eq. 8 and y is the

integration variable. The susceptance is different from its analog in the rigid-bodies radiation impedance (the reactance) in that the susceptance tends towards the hydrostatic stiffness in the zero frequency limit (Falnes, 2002), but similar in that it tends towards zero magnitude in the infinite frequency limit (Kurniawan et al., 2011).

Note that the only difference between implicitly solving for the radiation potential and explicitly solving for it (as is now available in WAMIT v7) is the use of the reciprocity relations. If WAMIT v7 were employed, the radiation conductance and susceptance would be direct output of the potential flow solver. All formalism proceeding and following is equally valid if these terms were found explicitly.

The coupling term H_j^u that arises from rigid-body oscillations resulting in internal free surface oscillations is found through

$$H_j^u(\omega) = -\iint_S \frac{\partial \varphi_j}{\partial z} dS = C_j + iJ_j \qquad 10$$

where the integral is taken over the internal free surface S and φ_j is the radiation potential of the body in each rigid-body mode j. Since it is only the radiation vertical velocity that is considered, axisymmetric devices with no cross-coupling (no heave-surge, no heave-pitch) will have only one contributing term—heave itself. This integration is computed discretely by obtaining the radiation vertical velocities $\frac{\partial \varphi_j}{\partial z}$ at each field point. The correct dimensionalization of the radiation velocity is given in WAMIT User Manual v7.0.

Finally it can be shown that $H_j^p = -H_j^u$ and hence, solving for H_j^p, which does explicitly require the radiation potential of the internal free surface, as identified in Eq. 2 is unnecessary.

The center of the internal water column will react to body motions around the COG. If the center of the free surface is not coincident with the COG then the following transformation vector is needed to account for the effect of body motions on the free surface:

$$\boldsymbol{T} = \begin{bmatrix} 0 & 0 & 1 & 0 & -r' & 0 \end{bmatrix}^{\mathrm{T}} \quad 11$$

where r' is identified in Fig. 1 A for the BBDB. It is clear from Fig. 2 A that $r' = 0$ for the axisymmetric device, and hence this transformation vector will not influence the solution.

A.2 Moonpool Hydrodynamic Results

The hydrodynamic parameters detailed in Sec. A.1.3 are found for wave frequencies spanning 0 to 2.5 rad/s in 0.01 rad/s intervals assuming infinite depth. The integral in Eq. 8 requires a sum over incident wave propagations. Therefore hydrodynamic parameters are found for 17 distinct wave-headings starting with incidence in the positive x-direction ($\beta = 0$) and increasing in intervals of $\pi/16$. Fig. 3 - Fig. 15 presented below highlight the wave – rigid-body – moonpool hydrodynamic interactions for the BBDB and axisymmetric devices. First the hydrodynamic terms are presented and then the hydrodynamic governing equation for the internal free surface, Eq. 5, is explored in more depth to highlight the new "coupled OWC" resonance frequency, $\omega_{coupledOWC}$, for a floating rigid-body with a moonpool.

A.2.1 BBDB Hydrodynamic Terms

Fig. 3 shows the characteristics of the excitation volume flow q resulting from the incident and diffracted velocity potentials. The primary peak, located at $\omega = 0.46$ rad/sec, is the piston resonance location for a fixed rigid-body (i.e. hydrodynamically uncoupled). The excitation volume flow has multiple amplitude peaks (shown in the inset figure) coupled with phase changes indicating that the BBDB has many other resonances (the sloshing resonances (Molin, 2001)) , likely attributable to the considerable internal surface area of this design. The three-dimensional free surface shapes of some of these resonances are explored more fully in Fig. 9 - Fig. 12.

Unlike axisymmetric rigid-bodies, asymmetric rigid-bodies exhibit cross-coupling between the heave-pitch and the heave-surge rigid-body modes. These cross-couplings manifest themselves in the radiation potential, φ_j, and hence will affect the natural resonances of the floating rigid-body

BBDB Design

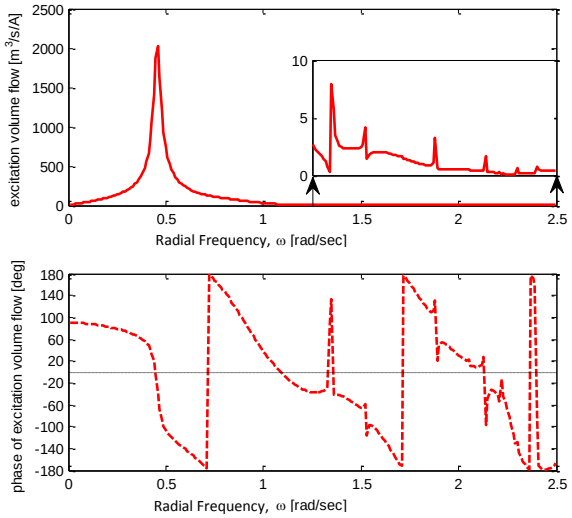

Fig. 3: Excitation volume flow, magnitude and phase, of the free surface in the BBDB.

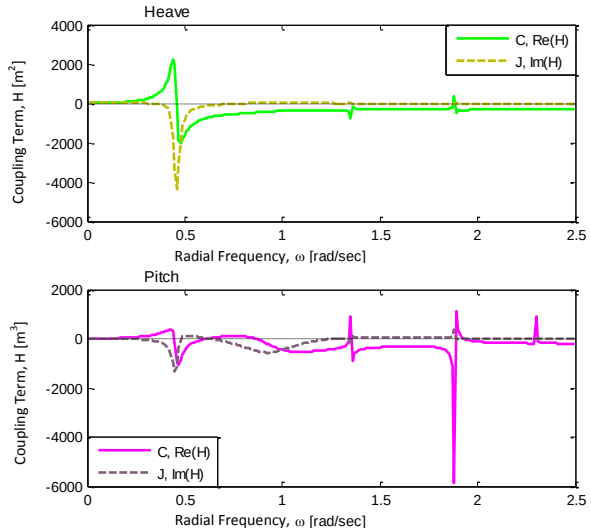

Fig. 4: BBDB coupling terms for heave and pitch motions of the body. Both modes exhibit strong coupling.

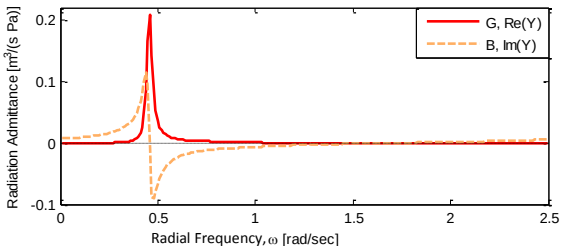

Fig. 5: Radiation conductance and susceptance of the internal free surface in the BBDB.

Axisymmetric Design

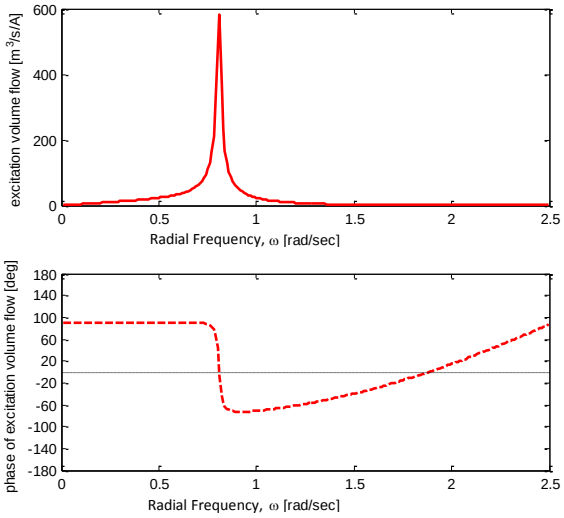

Fig. 6 Excitation volume flow, magnitude and phase, of the free surface in the axisymmetric device.

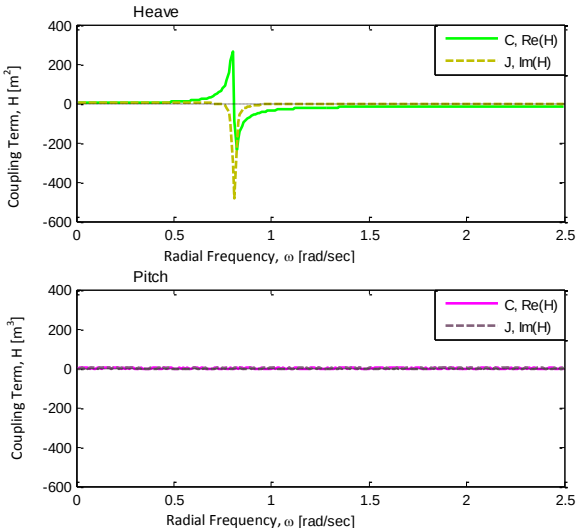

Fig. 7 Axisymmetric coupling terms for heave and pitch motions of the body. Only the heave coupling will occur in this device.

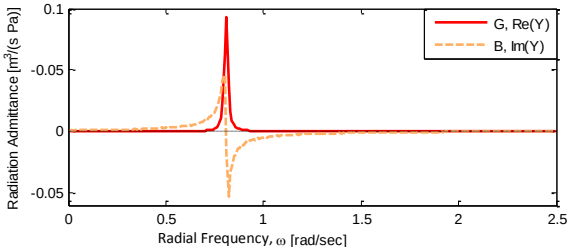

Fig. 8: Radiation conductance and susceptance of the internal free surface in the axisymmetric device.

(Newman, 1977). Additionally, since the hydrodynamic coupling between the rigid-body and moonpool is derived from the vertical radiation velocities, $\frac{\partial \varphi_j}{\partial z}$, there will be appreciable coupling magnitudes for these additional modes in surge and pitch. Fig. 4 shows the real and imaginary components of the heave and pitch coupling terms H_j^{μ}. The real parts of the coupling are tending towards stable and finite values whereas the imaginary parts are tending towards zero in the infinite frequency limit supporting the conclusions presented in (Kurniawan et al., 2011). Evidence of the sloshing resonances are also present in these coupling terms.

The radiation admittance for the BBDB is shown in Fig. 5. The zero and infinite frequency limits show the conductance tending towards zero while the susceptance tends towards zero in the infinite frequency limit and towards the hydrostatic stiffness in the zero frequency limit (Falnes, 2002). Furthermore, the first zero crossing of the susceptance is localized at ω_{piston}.

A.2.1.1 BBDB Free Surface Shapes

Since each internal free surface is represented by an array of field points, the three-dimensional shape of the free surface can be resolved as Molin (Molin, 2001) has done analytically for a fixed rigid-body. This representation allows for a three-dimensional visualization of the "piston" resonance as well as additional "sloshing" resonances. These additional resonances are identified by increasing the number of nodes (minimum amplitudes) in the free surface shape. Fig. 9 - Fig. 12 show the free surface profiles for the piston mode, ω_{piston}, and the 1st – 3rd longitudinal sloshing modes. These sloshing modes are at the 3rd, 4th, and 5th harmonics of ω_{piston}.

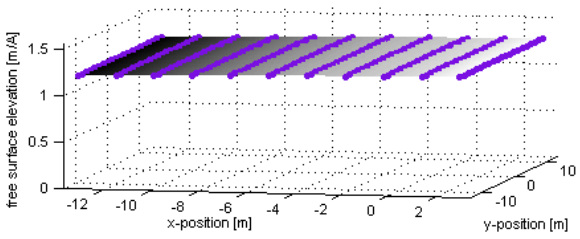

Fig. 9: Three-dimensional visualization of the free surface shape inside of the BBDB at ω_{piston} (ω=0.46 rad/sec). The purple dots are the locations of the field points identified in Fig. 1 B.

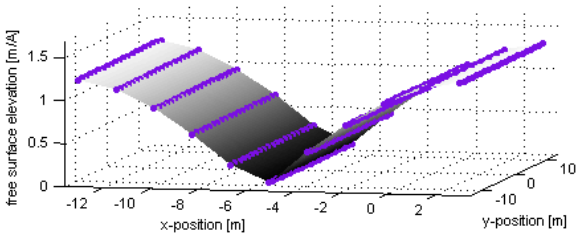

Fig. 10: Three-dimensional visualization of the free surface shape inside of the BBDB at the first longitudinal sloshing mode at ω=1.35~3* ω_{piston} rad/sec. The purple dots are the locations of the field points identified in Fig. 1 B.

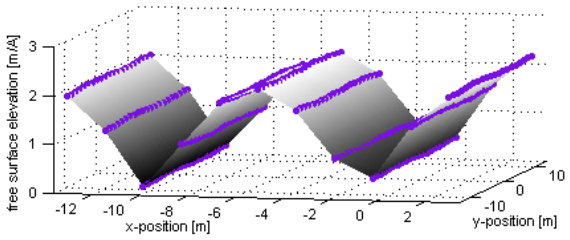

Fig. 11: Three-dimensional visualization of the free surface shape inside of the BBDB at the second longitudinal sloshing mode at ω=1.88~4* ω_{piston} rad/sec. The purple dots are the locations of the field points identified in Fig. 1 B.

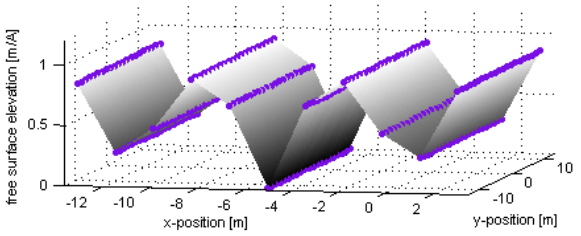

Fig. 12: Three-dimensional visualization of the free surface shape inside of the BBDB at the third longitudinal sloshing mode at ω=2.3~5* ω_{piston} rad/sec. The purple dots are the locations of the field points identified in Fig. 1 B.

A.2.2 Axisymmetric Hydrodynamic Terms

Fig. 6 shows the excitation volume flow q resulting from the incident and diffracted velocity potentials for the axisymmetric device. The primary magnitude peak, located at $\omega = 0.81$ rad/sec, is the piston resonance location for a fixed rigid-body (i.e. hydrodynamically uncoupled). It is clear from the phase results of the excitation volume flow that the axisymmetric device does not have any sloshing resonances within this frequency range.

Fig. 7 shows the real and imaginary components of the heave and pitch coupling terms H_j^u. Since this rigid-body is axisymmetric, there are no cross-coupling terms. Hence, the only coupling term is in the heave rigid-body mode. The radiation admittance for the axisymmetric device is shown in Fig. 8. The first zero crossing of the susceptance is located at ω_{piston}. The evaluation of the Hilbert Transformation (a standard MatLab operation) to obtain the radiation susceptance, as shown in Eq. 10, did not produce a smooth curve. Although there are many other methods that could be applied to solve the Kramers-Kronig relationship (Kurniawan et al., 2011), the data leading up to and away from the first zero crossing was instead smoothed to yield the result shown in Fig. 8. As with the BBDB, the trends in the infinite and zero frequency limits for both the coupling and radiation admittance terms show the anticipated and previously discussed behaviors.

A.2.3 Comparison of Hydrodynamic Terms

A striking difference between the two sets of hydrodynamic results is the location of ω_{piston}. Since these two devices possess grossly different water column lengths (35 m for the BBDB and 8.5 m for the axisymmetric device) this dissimilarity is anticipated. The considerable difference in the magnitude of the hydrodynamic terms between the two devices is also expected because of the differing internal surface areas (473 m^2 for the BBDB and 50 m^2 for the axisymmetric device).

Lastly, it is important to note that the asymmetry possessed by the BBDB inherently changes the coupling between the floating rigid-body and the vertical mode of the water column. By introducing asymmetry into this BBDB device design, the coupled natural resonance frequency of the water column will migrate due to the coupling with surge, heave, and pitch structural modes. This point is explored more fully in the next section.

A.2.4 Influence of the Floating Rigid-body on the Moonpool Natural Resonance Frequency

The piston natural resonance frequency was identified in the hydrodynamic terms for each of the modeled rigid-bodies. This moonpool resonance frequency will be seen in a fixed rigid-body (no

wave-activated rigid-body motions) when open to atmosphere. The governing equation for this total hydrodynamic volume flow is given by

$$Q_{TH} = qA. \quad 12$$

However, when a moonpool open to atmosphere is contained within a rigid-body that is allowed to float, the governing equation for the total hydrodynamic volume flow is given by Eq. 5. In the case of the hydrodynamically coupled asymmetric BBDB, the total hydrodynamic volume flow is given by

$$Q_{TH} = qA - (H_1^u u_1 + H_3^u u_3 + H_5^u u_5) \quad 13$$

where u_1, u_3, and u_5 are the velocity response amplitude operators that predict the floating rigid-body's response at each frequency. While in the case of the hydrodynamically coupled axisymmetric design, the total hydrodynamic volume flow is given by

$$Q_{TH} = qA - (H_3^u u_3). \quad 14$$

It becomes clear by comparing Eq. 12 with Eq. 13 and 14 that the hydrodynamically coupled devices will: 1) exhibit rigid-body characteristics and 2) have a new coupled natural resonance location. Additionally, by comparing Eq. 13 and Eq. 14 it is clear that asymmetric rigid-body profiles will have a larger effect on the coupled natural resonance location because they have non-zero H_1^u and H_5^u terms. Fig. 13 - Fig. 14 compare the total hydrodynamic volume flow for the BBDB and axisymmetric designs when fixed (hydrodynmically uncoupled) and when floating (hydrodynamically coupled). Both the magnitudes and phases are shown in these comparisons to highlight resonance frequencies.

Focusing first on the BBDB, as shown in Fig. 13, the main difference between the hydrodynamically coupled and uncoupled results lies in the number of peaks. The hydrodynamically coupled device exhibits peaks at three frequencies: the structurally defined $\omega_{heave}$and ω_{pitch}, and the coupled oscillating water column resonance $\omega_{coupledOWC}$. The heave and pitch natural resonance frequencies align with the expectations set forth in Eq. 4. Additionally, these resonances exhibit a strong phase change as would be expected. Clearly, the frequency of the coupled oscillating water column

natural resonance has migrated substantially from ω_{piston} predicted for a fixed rigid-body. A gradual change in phase is associated with $\omega_{coupledOWC}$ indicating a damped system.

BBDB Design

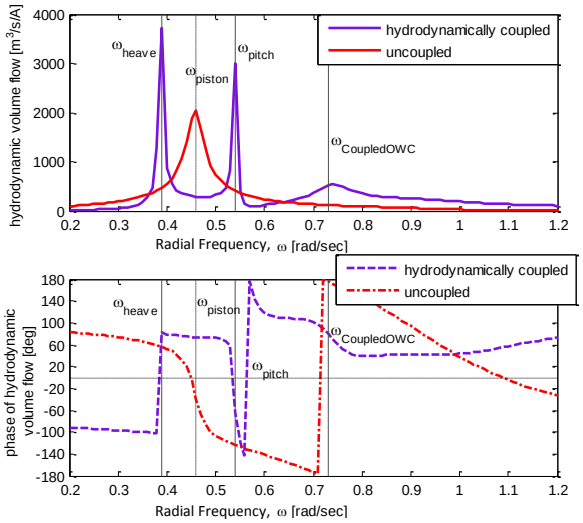

Fig. 13. Confirmation of the migration of the water column natural resonance due to hydrodynamic coupling for the BBDB.

Axisymmetric Design

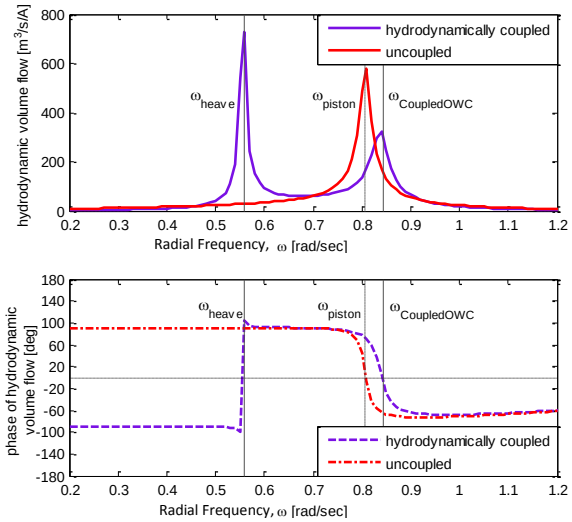

Fig. 14. Confirmation of the migration of the water column natural resonance due to hydrodynamic coupling for the axisymmetric device.

Focusing on the axisymmetric device, Fig. 14, a large shift in the oscillating water column natural resonance is not observed. In fact the shift is so small that it would be possible to miss the influence of the rigid-body on the internal free surface altogether. Significantly, as observed with the BBDB design, the hydrodynamically coupled device exhibits peaks at the expected two frequencies: the structural ω_{heave}, and the coupled oscillating water column resonance $\omega_{coupledOWC}$. These resonance locations are corroborated with phase changes.

A marine vessel possesses more of the asymmetric characteristics of the BBDB. However, a marine vessel also mimics the axisymmetric device in that the surface area of the moonpool is small. Hence although the natural resonance of the moonpool in marine vessels is technically migrating, this phenomena has not been reported on extensively (experimentally or analytically) because for the majority of vessels the magnitude of the migration is so small that is has not been noticed. An exception to this is the work completed by Maisondieu (Maisondieu and Ferrant, 2003) on the Wellhead Barge.

The Wellhead Barge is similar to a BBDB in that this barge contains an unusually large moonpool (~45% of the length and ~33% of the beam). They experimentally found the hydrodynamically coupled moonpool natural resonance to lie at 0.92 Hz whereas the predicted hydrodynaically uncoupled piston natural resonance was 0.798 Hz. Additional experimental work completed by Yang (Yang and Kwon, 2013) shows that there is a migration between fixed and floating moonpool natural resonance from 1.12 Hz to 1.20 Hz. Neither of these observations were directly addressed with an analytic explanation.

By explicitly employing the hydrodynamic coupling terms between the floating rigid-body and a moonpool open to atmosphere as is done in Eq. 5, an analytic explanation for the migration of the moonpool natural resonance frequency is obtained. In the next section, more experimental results will be presented to further validate the coupled OWC resonance.

4.4.1 Experimental Verification of $\omega_{coupledOWC}$ for a Fully Vented BBDB

The BBDB device while fully vented to atmosphere was tested in the Hydraulic Marine Research Center wave basin at the University College Cork in Ireland. A Froude scaling factor of 50 was applied to the device to match the wave environment in the wave basin. The BBDB was situated in a backward facing manner, secured with two mooring lines, and ballasted to obtain the desired draft. Period sweeps of regular small amplitude waves were run at the device. All waves were pre-calibrated and these wave heights were used in the calculation of the Response Amplitude Operators (RAOs) shown below in Fig. 15.

The rigid-body motions and the internal free surface elevation (FSE) were tracked in three dimensions with a Qualisys system ("Qualisys Motion Capture Systems," n.d.). In the basin both the port and starboard (stbd) side FSEs were measured. Note that this experimental data was not used to calibrate the viscous losses in the numerical model; the losses in the numerical model were assumed as discussed in Sec. B.2.1.

Fig. 15 compares the experimentally determined RAOs with the predicted results (at full scale) for a fully vented air chamber. The FSE plots (both absolute and relative to the rigid-body) confirm the predicted hydrodynamcially coupled OWC resonance frequency by exhibiting a large response from both the port and starboard measurements at that frequency. Further, the experimental volume flow RAO confirms the predicted shape. There is no evidence of $\omega_{piston} = 0.46$ rad/sec in the experimental data.

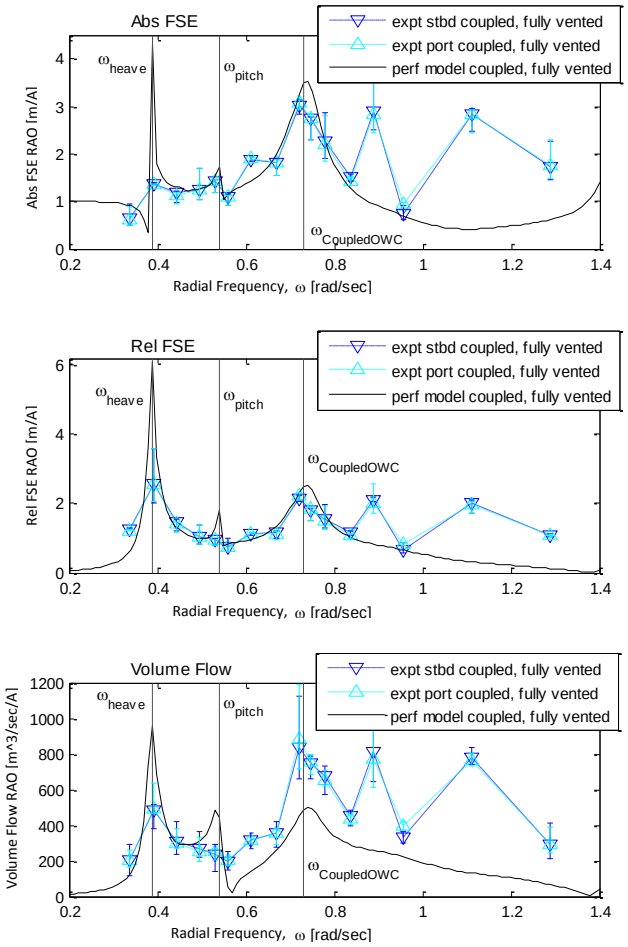

Fig. 15 Experimental verification of $\omega_{copuledOWC}$ through RAOs of absolute FSE, relative FSE, and volume flow for a fully vented BBDB.

At large radial frequencies, the predicted and experimentally determined values begin to diverge in all of the comparisons. This is probably due to the difficulty of producing high quality, short period waves in wave basins, the fact that sloshing modes on the internal free surface are also expected

at these higher frequencies (as anticipated from Sec. A.2.1.1 and visually present at these high frequency values), and the un-calibrated viscous losses assumed in the numerical model.

Regardless of these issues, Fig. 15 show that there is no response at ω_{piston} and there is a large response at $\omega_{coupledOWC}$ thus experimentally verifying the predicted $\omega_{coupledOWC}$ for the BBDB.

Section B.

B.1 Linked Governing Equations for an OWC

The performance model for floating OWCs not only considers the coupled wave – rigid-body – moonpool interactions described above, but also links the rigid-body to the OWC through a control strategy implemented with a representative PCC. A linear relationship between pressure and flow is assumed in this performance model. The most common turbine capable of producing this relationship is a Wells Turbine (Gato and Falcão, 1988). The Wells Turbine is self-rectifying and hence rotates only in one direction when subject to bidirectional air flow. A resistive damping term R_{load}, which is governed by the diameter and rotation rate of the turbine, is used to improve the performance of the device in regular and irregular wave environments. Only the regular wave performance of the devices presented in Fig. 1 and Fig. 2 will be investigated using the linked linear frequency-domain model described below. The BBDB performance in irregular waves is detailed in (Bull, 2014).

The linked governing equations are subject to Newton's Second Law and take the following abstract form:

$$Total_{force/flow} = Hydrodynamic_{force/flow} + Hydrostatic_{force} + Viscous_{force/flow} + Control_{flow} + Mooring_{force} \quad (15)$$

where the subscripts identify the applicability of the abstract term to either the body through force or the internal water column through flow. Since air is highly compressible, accurate predictions of the total air flow through the turbine requires a linear representation of this compressibility. The hydrodynamic coupling described above enters the force balanced equation through the

$Hydrodynamic_{force/flow}$ term. The hydrostatic response of the wave-activated rigid-body must be explicitly included in the total force equation, while this is already present in the $Hydrodynamic_{flow}$ term. The rigid-body and the internal water column will both have associated linearized viscous losses. The PCC control term is accounted for in the internal water column governing equation. Finally, the mooring restoring force is accounted for in the body's governing equation.

Given the generalized form of the linked governing equations in Eq. 15 the specific coupled governing equations that detail the motions of the rigid-body and free surface are calculated in matrix notation using

$$\begin{pmatrix} \boldsymbol{f} \\ q \end{pmatrix} A = \begin{pmatrix} \boldsymbol{Z}_i & -\boldsymbol{H}_i \\ \boldsymbol{H}_i^T & Y_i + \dfrac{1}{R_{load}} \end{pmatrix} \begin{pmatrix} \boldsymbol{u} \\ p \end{pmatrix} \tag{16}$$

where the bolded quantities are matrices or column vectors and

$$\boldsymbol{Z}_i = \boldsymbol{b} + \boldsymbol{b}_{vis} + i\omega \left(\boldsymbol{m} + \boldsymbol{a} - \frac{(\boldsymbol{C} + \boldsymbol{K})}{\omega^2} \right), \tag{17}$$

$$\boldsymbol{H}_i = \boldsymbol{H} + \boldsymbol{T}S, \text{ and} \tag{18}$$

$$Y_i = \left(G + \left(\frac{1}{R_{vis}} \right) \right) + i \left(B + \frac{\omega \forall_o}{\gamma p_{atm}} \right). \tag{19}$$

The subscript i indicates that the purely hydrodynamic terms have been expanded to acknowledge the full mechanical system (e.g. moving from radiation impedance to mechanical impedance). In Eq. 16 the velocity of the body $\boldsymbol{u}$ and the pressure in the internal air chamber p are united through the hydrodynamic coupling term $\boldsymbol{H}_i$. $\boldsymbol{H}$ is modified by the transformation vector $\boldsymbol{T}S$ to become $\boldsymbol{H}_i$ which accounts for the relativized pressure-volume flow at the center of the free surface (see Eq.'s 11 and 18).

The velocity response of the body per unit wave amplitude, $\boldsymbol{u}/A$ (the velocity RAO), is governed by the hydrodynamic coupling term and the traditional wave – rigid-body hydrodynamic terms: the

radiation damping $\boldsymbol{b}$ and added mass $\boldsymbol{a}$, the excitation force $\boldsymbol{f}$, as well as the restoring forces $\boldsymbol{C}$, mooring forces $\boldsymbol{K}$, and mass of the rigid-body $\boldsymbol{m}$.

The relative pressure RAO, ${}^{p}/_{A}$, is also determined through coupling and linking, in addition to the wave-moonpool hydrodynamic terms described above. Air compressibility is specified through the initial volume $\forall_o$, the ratio between the constant-pressure and constant-volume specific enthalpies for air $\gamma = 1.4$, and the atmospheric pressure p_{atm}. The relative volume flow RAO may be calculated from:

$$Q_T = qA - Y_i p - \boldsymbol{H}_i^T \boldsymbol{u} = \frac{p}{R_{load}} \tag{20}$$

where the last equality acknowledges that the wave-activated rigid-body is now linked to the free surface through a linear PCC with the ability to implement a control strategy to increase the absorbed power.

The power absorbed by the coupled and linked device is dependent upon the R_{load} applied at the air turbine. The average pneumatic power available to the turbine from the air-column is the product of the relative pressure in the air-chamber and the relative volume flow, as shown by Falnes (Falnes, 2002)

$$\langle P \rangle = \overline{p(t)Q_T(t)} = \frac{1}{2} Re\{pQ_T^*\}. \tag{21}$$

This general form of the average pneumatic power will be used in the following sections to determine the linked power performance in regular waves.

B.2 Linked Performance in Regular Waves

In monochromatic waves, the average pneumatic power in Eq. 21 simplifies to

$$\langle \mathrm{P} \rangle = \frac{1}{2} \frac{1}{R_{load}} |p|^2 = \frac{1}{2} R_{load} |Q_T|^2. \tag{22}$$

It is clear that the magnitude of the resistive damping term will impact the pneumatic power available to the turbine by influencing both the motion of the body and the motion of the water column.

The optimal resistive damping term can be found from the solution to the following optimization condition

$$\frac{\partial \langle \mathrm{P} \rangle}{\partial R_{load}} = 0. \tag{23}$$

where $\langle P \rangle$ is the average power presented in Eq. 22. Application of the optimization condition presented in Eq. 23 results in the following analytic form of the frequency dependent optimal resistive damping (as first presented by (Bull and Johnson, 2013)):

$$R_{l_{opt}} = \frac{1}{\left| Y_i + \boldsymbol{H}_i^T \boldsymbol{Z}_i^{-1} \boldsymbol{H}_i \right|}. \tag{24}$$

Eq. 24 gives the frequency dependent optimal resistive damping values for a floating OWC. If the rigid-body were fixed, the optimal R_{load} would consist of only the first term in Eq. 24. However, since the body is floating and is coupled to the internal free surface, the optimal resistive damping must reflect the contribution from the floating rigid-body. Hence, the additional term relating to the magnitude of coupling $\boldsymbol{H}_i$ and the mechanical impedance $\boldsymbol{Z}_i$ of the rigid-body in the analytic form of $R_{l_{opt}}$ is reasonable. Inserting Eq. 24 into Eq. 22 produces the maximum pneumatic power in regular waves.

B.2.1 Linked Performance Results in Regular Waves

Only a single heading, $\beta = 0$, is analyzed to estimate performance. Since the BBDB is a directionally dependent device, the metrics presented in the following sections will highlight the best possible performance. Additionally the mechanical efficiency of the turbine is not accounted for, again resulting in overly optimistic performance predictions.

The linear potential flow predictions must be reduced to reflect the reality of viscous losses. These losses will result in decreased responses to the incident wave environment; the RAO magnitudes will be reduced from unrealistic values at resonance to reasonable levels. Constant (and diagonal when applicable) damping values for both the rigid-body and the free surface are applied across all frequencies in order to reduce the RAO responses. The critical damping coefficient of a second order

ordinary differential equation (like the force side presented in Eq. 15) is generally given by $2\sqrt{(mass)(spring)}$. This relationship is used to determine the rigid-body-viscous losses. Specifically, for the presented solutions $b_{vis} = 0.02\left(2\sqrt{M_{tot}c_{tot}}\right)$; M_{tot} is the physical mass in combination with the infinite frequency added mass and c_{tot} is the total restoring force (hydrostatic plus mooring). No mooring restoring force is applied ($\boldsymbol{K} = 0$). The author knows of no equivalent physical basis on which to select the water column-viscous losses. The presented solutions use and $R_{vis}^{-1} = 0.01(\max(G))$.

In summary both devices have air chamber heights of 10m and their rigid-body-viscous losses are 2% of the critical damping coefficient while their water column-viscous losses are 1% of the maximum radiation conductance. Although there may be more physical mechanisms of selecting the viscous losses, the effect will be the same—a reduction of the RAO magnitudes. Fig. 16 - Fig. 26 presented below highlight the dynamic and power performance of each of the devices in regular waves.

B.2.1.1 BBDB

Fig. 16 compares the analytic expression of $R_{l_{opt}}$ from Eq. 24 as a function of frequency to a numeric optimization; the comparison reveals a perfect match. Since both the rigid-body motions and the free surface are accounted for in the relative pressure term, the profile of $R_{l_{opt}}$ experiences multiple distinct minima corresponding to natural resonances for the coupled device. The structural resonance frequencies and the coupled OWC resonance frequency are identified in Fig. 16 for clarity with solid vertical lines. Between these minima, $R_{l_{opt}}$ increases, resulting in three resistive damping peaks identified with dashed lines for clarity. These vertical lines, both the solid and dashed, are mimicked in the rest of the regular wave performance results to highlight the influence of the resonances and resistive control on the results.

Fig. 17 compares the linked and unlinked RAOs for heave, pitch, and the absolute FSE when $R_{l_{opt}}$ is applied at each frequency. This comparison highlights the influence of the control strategy on the dynamic response of the device. The linked RAOs exhibit the unlinked natural resonances as would

BBDB Design

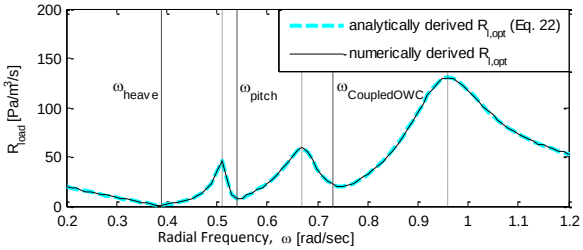

Fig. 16: Comparison of analytically derived and numerically obtained optimal resistive damping $R_{l_{opt}}$ for the BBDB.

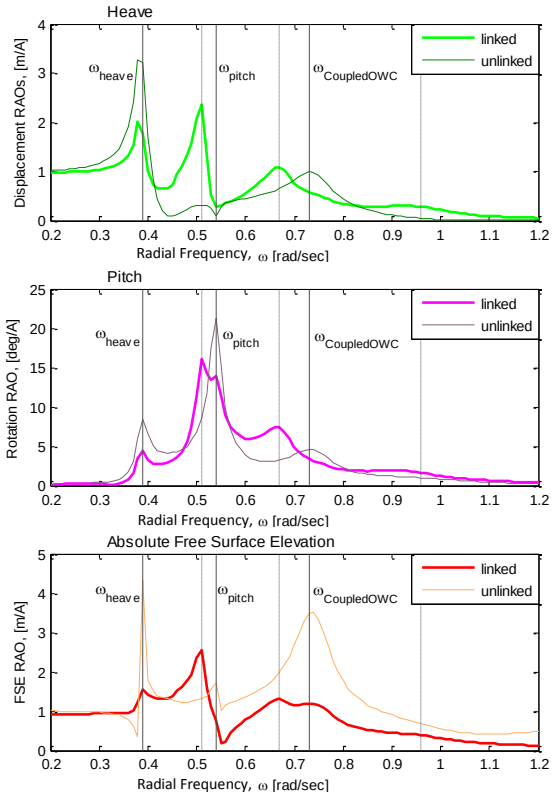

Fig. 17: RAOs for heave, pitch, and the absolute free surface elevation when a turbine with $R_{l_{opt}}$ is applied in the linked case and when there is no turbine in the unlinked case.

Axisymmetric Design

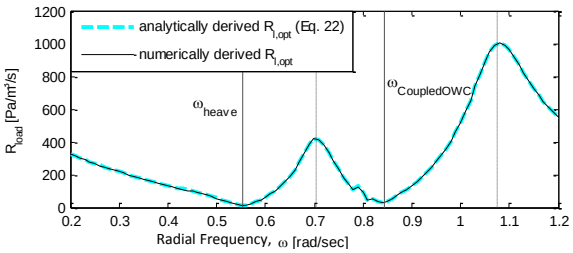

Fig. 18: Comparison of analytically derived and numerically obtained optimal resistive damping $R_{l_{opt}}$ for an axisymmetric floating OWC.

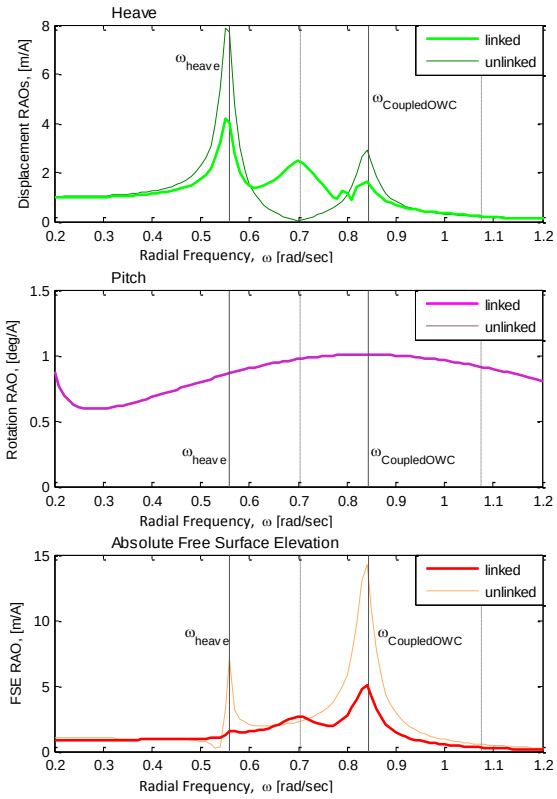

Fig. 19: RAOs for heave, pitch, and the absolute free surface elevation when a turbine with $R_{l_{opt}}$ is applied in the linked case and when there is no turbine in the unlinked case.

BBDB Design

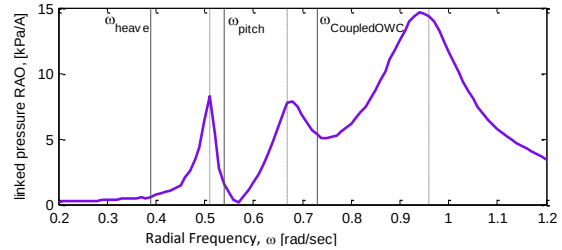

Fig. 20: RAO of relative linked pressure with $R_{l_{opt}}$ applied.

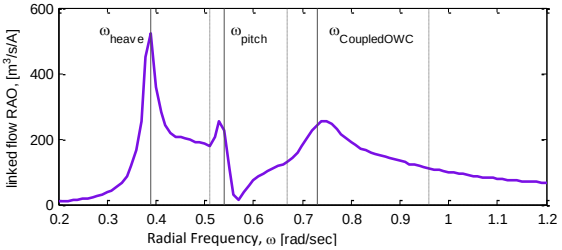

Fig. 21: RAO of relative linked flow with $R_{l_{opt}}$ applied.

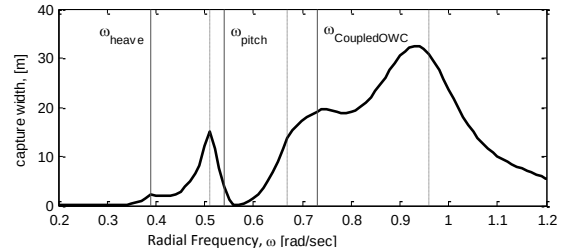

Fig. 22: Capture width for an asymmetric floating OWC with $R_{l_{opt}}$ applied at each frequency.

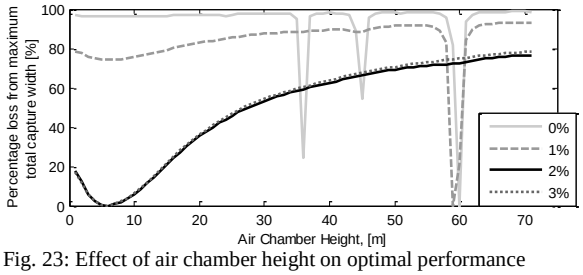

Fig. 23: Effect of air chamber height on optimal performance (black line corresponds to baseline rigid-body-viscous losses). A constant volume flow-viscous loss of 1% is applied while rigid-body-viscous losses are altered from 0% to 3% of the critical damping coefficient.

Axisymmetric Design

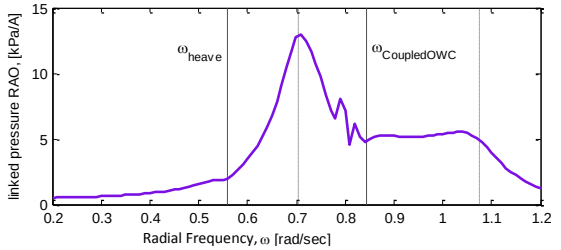

Fig. 24: RAO of relative linked pressure with $R_{l_{opt}}$ applied.

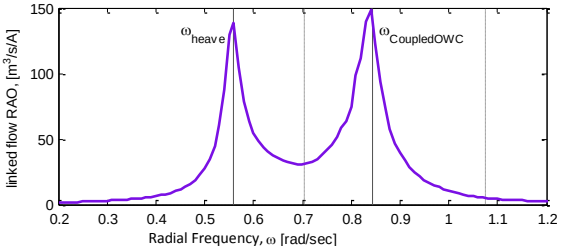

Fig. 25: RAO of relative linked flow with $R_{l_{opt}}$ applied.

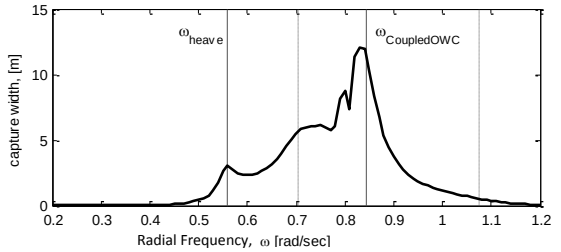

Fig. 26: Capture width for an axisymmetric floating OWC with $R_{l_{opt}}$ applied at each frequency.

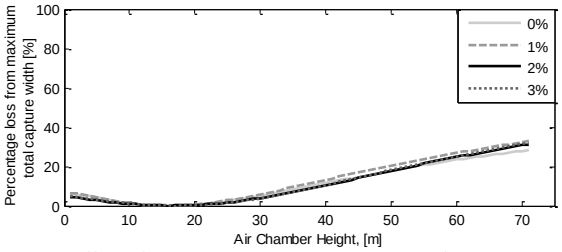

Fig. 27: Effect of air chamber height on optimal performance (black line corresponds to baseline rigid-body-viscous losses). A constant volume flow-viscous loss of 1% is applied while rigid-body-viscous losses are altered from 0% to 3% of the critical damping coefficient.

be expected since $R_{l_{opt}}$ is minimal at these locations. However, the linked RAOs also exhibit additional peaks that correspond to the peaks seen in $R_{l_{opt}}$. This is a direct result of the coupling that exists between the rigid-body and the enclosed water column.

The relative linked pressure is shown in Fig. 20 and the relative linked volume flow in Fig. 21. Inspection of these figures reveals that the peaks in pressure correspond to the locations of increased resistive damping, while the peaks in relative volume flow correspond to resonances in the system. This inverse partnership between pressure and flow is expected: when the device is at resonance there will be large volume flow, otherwise $R_{l_{oad}}$ will be used to increase the pressure in the air-chamber.

The capture width is defined as the ratio of absorbed power to the incident wave power per unit width of the wave crest (or wave power flux) for that frequency. The capture width of this device, with $R_{l_{opt}}$ applied at each frequency, is shown in Fig. 22. Both the heave and the coupled OWC resonances contribute to the capture width. The pitch natural resonance is not detectable, but it is likely that it has been subsumed into the prior peak. The three peaks in $R_{l_{opt}}$ values result in large capture widths.

The spring-like effect of air compressibility has been shown by Sarmento and Falcão (Sarmento and Falcão, 1985) to effect OWC power performance. Fig. 23 studies the effect of linearized air compressibility on device performance by changing the total volume of air enclosed within the chamber. This study is presented using a new metric to evaluate distinct volumes against one another. Since the capture width profile decays to zero for both low and high frequencies the “area under the capture width curve” can be used as a proxy for the best performing device. In this study each air chamber height is modeled and the “area under the capture width curve” is calculated. The percentage loss from the maximum ‘area under the capture width curve’ is then used to normalize all values.

Employing the metric described above, Fig. 23 investigates the influence of air chamber height and rigid-body-viscous losses. The solid black line represents the baseline rigid-body-viscous loss (2% of the critical damping coefficient) while the other lines indicate the effect of differing rigid-body-viscous losses. For the baseline case, the optimal height is 6m. It is clear that the optimal air chamber height is sensitive to the selected rigid-body-viscous losses exhibiting a strongly multi-peaked profile in Fig. 23 for small losses. This multi-peaked behavior is likely the result of appreciable motions in the six rigid-body

degrees of freedom as opposed to only having motion in a single degree of freedom. This behavior suggests it is important for designers of BBDB's to obtain accurate estimates of the viscous losses and to evaluate the optimal air chamber height carefully.

B.2.1.2 Axisymmetric

Much of the same general rigid-bodies seen for the BBDB are also seen in the axisymmetric design. Fig. 18 shows the analytically derived expression of $R_{l_{opt}}$ from Eq. 24 for the axisymmetric design. The jagged behavior seen in $R_{l_{opt}}$ around $\omega = 0.8$ rad/sec, is due to the inaccurate Hilbert transformation, as discussed in Sec. A.2.2; this behavior is propagated into the dynamic responses in the later figures. Again, since both the rigid-body motions and the free surface are accounted for in the relative pressure term, multiple distinct minima corresponding to the heave and coupled OWC resonances are seen and are identified with solid vertical lines. The dashed vertical lines occurring between these minima correspond to the resistive damping peaks. These vertical lines, both solid and dashed, are mimicked in the rest of the corresponding axisymmetric performance figures.

Fig. 19 compares the linked and unlinked RAOs for heave, pitch, and the absolute FSE when $R_{l_{opt}}$ is applied at each frequency, again highlighting the influence of the control strategy on the dynamics of the device. Unlike the BBDB there is no cross-coupling between pitch and heave and no pitch influence on the coupled OWC location; additionally, the pitch natural frequency (identified in Table III) is outside of the frequency range shown. However, like the BBDB, it is clear that the linked RAOs exhibit more peaks than the unlinked RAOs, and those additional peaks correspond to the peaks seen in $R_{l_{opt}}$ (Fig. 18). These results match those found by Alves (Alves, 2012) who, in contrast to this work, utilized the method of generalized modes to determine the wave – rigid-body – moonpool interactions in his performance model.

The inverse partnership seen for the BBDB between linked relative pressure and linked relative flow in Fig. 17 and Fig. 18 are shown in Fig. 24 and Fig. 25 for the axisymmetric device. The capture

width of the axisymmetric device is shown in Fig. 26. Interestingly, the resonances (heave and coupled OWC) contribute the most to the capture width for the axisymmetric device, whereas for the BBDB, the peaks in $R_{l_{opt}}$ appeared to be the dominant contributors.

The effect of linearized air compressibility on device performance due to changing air chamber height is shown in Fig. 27. Again, using the metric percentage loss from the maximum "area under the capture width curve" it is clear that the location of the optimal height is 16 m. In contrast to the BBDB, for this axisymmetric device the rigid-body-viscous losses do not influence the number of peaks in the profile, nor the optimal height.

3. Conclusions

The fundamental interactions between waves, a floating rigid-body, and a moonpool that is selectively open to atmosphere or enclosed to purposefully induce pressure fluctuations are investigated. By directly modeling the free surface of the moonpool and the rigid-body with linear potential flow theory the hydrodynamic coupling between the rigid-body and the moonpool elucidates how the moonpool natural resonance frequency is altered when enclosed within a floating rigid-body as opposed to a fixed rigid-body.

Two geometries were investigated within this study to represent both the marine vessels with moonpools and OWC WEC devices. Marine vessels with moonpools are typically asymmetric with small surface area moonpools and are open to the atmosphere above. The asymmetric BBDB mimics the rigid-body profile of marine vessels, while the axisymmetric design contains moonpool with a small surface area. The dimensions and structural parameters of both non-optimized devices are detailed within the study.

The hydrodynamic parameters relating to the internal water column are calculated using reciprocity relations on an array of field points defining the internal free surface for both the asymmetric BBDB device and the axisymmetric device. The hydrodynamic coupling $\boldsymbol{H}_j^u$ terms were derived for each

of the geometries and highlight the importance of structural cross-coupling (heave-pitch and heave-surge) in asymmetric geometries.

The formalism developed in this paper allows for insight into why the piston resonance is not experimentally obtained for floating rigid-bodies with open moonpools. In Section A the two designs were studied while the moonpools were open to atmosphere. Once the hydrodynamic coupling $\boldsymbol{H}_j^{\mu}$ is explicitly included, it is clear that the moonpool will 1) exhibit rigid-body characteristics and 2) have a new coupled natural resonance location. These conclusions are supported not only through the analytical equations, but also through experimental work presented in this paper and experimental work completed by (Maisondieu and Ferrant, 2003) and (Yang and Kwon, 2013). The migration of the moonpool resonance is pronounced for asymmetric rigid-bodies and moonpools with large areas.

Narrowing the focus to renewable energy devices, the air chamber is enclosed and a 3-dimensional, linear, frequency-domain performance model that links the rigid-body to the OWC is detailed. The performance model is exercised on devices in regular waves using the calculated hydrodynamic parameters. The air within the enclosed chamber is modeled as a linearly compressible system, and viscous losses are applied to the rigid-bodies and their air chambers.

A linear representation of a power conversion chain is used and an analytic expression to determine the optimal $R_{l_{oad}}$ in regular waves for any floating OWC is presented. This expression differs from the standard fixed OWC expression, i.e. hydrodynamically uncoupled, by terms relating to the magnitude of hydrodynamic coupling $\boldsymbol{H}_i$ and the mechanical impedance $\boldsymbol{Z}_i$ of the rigid-body. When the optimal resistive load is exercised within the performance model, the natural resonances of the coupled system are preserved and additional linked peaks are identified. Results of the device motion, internal water column motion and resulting pressure are presented. The capture width of the BBDB is shown to have a broader frequency response than that of the axisymmetric device. Regular wave performance

(power and dynamics) of the axisymmetric device match predictions made by Alves (Alves, 2012) using an alternative method to model the internal free surface hydrodynamic parameters.

Acknowledgements

This work arose from many helpful conversations, most notably with Erick Johnson, Marco Alves, Paul Palo, and Adi Kurniawan. The staff at HMRC were instrumental in obtaining the experimental data presented here. Dale Berg kindly offered editorial assistance. And finally, I would like to acknowledge the thoughtful questions and comments from the reviewers.

This work was funded by the U.S. Department of Energy's Wind and Water Power Technologies Office. Sandia National Laboratories is a multi-program laboratory managed and operated by Sandia Corporation, a wholly owned subsidiary of Lockheed Martin Corporation, for the U.S. Department of Energy's National Nuclear Security Administration under contract DE-AC04-94AL85000.

Bibliography

Alves, M.A. de A., 2012. Numerical Simulation of the Dynamics of Point Absorber Wave Energy Converters using Frequency and Time Domain Approaches (PhD). Universidade Técnica de Lisboa, Instituto Superior Técnico.

Bull, D., 2014. Pneumatic Performance of a non-axisymmetric floating oscillating water column wave energy conversion device in random waves, in: Proceedings of the 2nd Marine Energy Technology Symposium. Presented at the Marine Energy Technology Symposium, Seattle, WA, USA.

Bull, D., Johnson, E., 2013. Optimal Resistive Control Strategy for a Floating OWC Device, in: Proceedings of the 11th European Wave and Tidal Energy Conference. Presented at the EWTEC, Aalborg, Denmark.

Bull, D., Smith, C., Jenne, D.S., Jacob, P., Copping, A., Willits, S., Fontaine, A., Brefort, D., Copeland, G., Gordon, M., Jepsen, R.A., 2014. Reference Model 6 (RM6): Oscillating Water Column Device (SAND Report No. SAND2014-18311). Sandia National Laboratories.

Evans, D.V., 1982. Wave-Power Absorption by Systems of Oscillating Surface Pressure Distributions. J. Fluid Mech. 114, 481–499. doi:10.1017/S0022112082000263

Evans, D.V., 1978. The Oscillating Water Column Wave-energy Device. IMA J. Appl. Math. 22, 423–433. doi:10.1093/imamat/22.4.423

Falcão, A.F.O., Henriques, J.C.C., Cândido, J.J., 2012. Dynamics and optimization of the OWC spar buoy wave energy converter. Renew. Energy 48, 369–381. doi:10.1016/j.renene.2012.05.009

Falnes, J., 2002. Ocean Waves and Oscillating Systems. Cambridge University Press, New York.

Gato, L.M.C., Falcão, A.F.O., 1988. Aerodynamics of the wells turbine. Int. J. Mech. Sci. 30, 383–395. doi:10.1016/0020-7403(88)90012-4

Gomes, R.P.F., Henriques, J.C.C., Gato, L.M.C., Falcão, A.F.O., 2012. Hydrodynamic optimization of an axisymmetric floating oscillating water column for wave energy conversion. Renew. Energy 44, 328–339. doi:10.1016/j.renene.2012.01.105

Hong, D., Hong, S., Hong, S., 2004. Numerical study on the reverse drift force of floating BBDB wave energy absorbers. Ocean Eng. 31, 1257–1294.

Imai, Y., Toyota, K., Nagata, S., Setoguchi, T., Takao, M., 2011. An Experimental Study on Generating Efficiency of a Wave Energy Converter" Backward Bent Duct Buoy, in: 9th European Wave and Tidal Energy Conference. Presented at the EWTEC.

Kurniawan, A., Hals, J., Moan, T., 2011. Modeling And Simulation Of A Floating Oscillating Water Column, in: Proceedings of the ASME 2011 30th International Conference on Ocean, Offshore and Arctic Engineering. Presented at the American Society of Mechanical Engineers, Rotterdam, The Netherlands, pp. 395–406.

Lee, C.H., Newman, J.N., Nielsen, F.G., 1996. Wave interactions with an oscillating water column, in: Proceedings International Offshores and Polar Engineering Conference. Los Angeles.

Lee, C.H., Nielson, F.G., 1996. Analysis of oscillating-water column device using a panel method. Presented at the 11th International Workshop on Water Waves and Floating Bodies, Hamburg Germany.

Maisondieu, C., Ferrant, P., 2003. Evaluation of the 3D Flow Dynamics in a Moonpool, in: The Proceedings of the Thirteenth (2003) International Offshore and Polar Engineering Conference. Presented at the International Society of Offshore and Polar Engineers, Honolulu, Hawaii, USA.

Maisondieu, C., Le Boulluec, M., 2001. Flow dynamics in a moon-pool Experimental and numerical assessment, in: Proc OMAE'2001 Conference. Presented at the OMAE, Rio de Janeiro, Brazil.

Masuda, Y., Yamazaki, T., Outa, Y., McCormick, M., 1987. Study of backward bent duct buoy, in: OCEANS'87. Presented at the IEEE, pp. 384–389.

Molin, B., 2001. On the piston and sloshing modes in moonpools. J. Fluid Mech. 430, 27–50.

MultiSurf, n.d. . AeroHydro, Inc., Southwest Harbor, Maine.

Newman, J.N., 1977. Marine hydrodynamics. MIT Press.

Ocean Energy Ltd., n.d. Ocean Energy OEBuoy: A Backward Bent Duct Design. [WWW Document]. URL http://www.oceanenergy.ie/ (accessed 4.4.13).

O.M. Faltinsen, 1990. Sea Loads on Ships and Offshore Structures, Cambridge Ocean Technology. Cambridge University Press.

Qualisys Motion Capture Systems [WWW Document], n.d. URL http://www.qualisys.com/ (accessed 4.23.14).

Reference Model Project. Sandia National Laboratories. [WWW Document], n.d. . Overv. Ref. Model Proj. URL http://energy.sandia.gov/rmp (accessed 4.30.14).

Sarmento, A.J.N.A., Falcão, A.F.O., 1985. Wave generation by an oscillating surface-pressure and its application in wave-energy extraction. J. Fluid Mech. 150, 467–485. doi:10.1017/S0022112085000234

Smith, C., Bull, D., Willits, S., Fontaine, A., 2014. Optimization and average annual power predictions of a Backward Bent Duct Buoy oscillating water column device using a Wells Turbine, in: Proceedings of the 2nd Marine Energy Technology Symposium. Presented at the Marine Energy Technology Symposium, Seattle, WA, USA.

SolidWorks 3D CAD Design Software, n.d. . Dassault Systèmes SolidWorks Corp.

Suzuki, M., Kuboki, T., Nagata, S., Setoguchi, T., 2011. Numerical Investigation of 2D Optimal Profile of Backward-Bent Duct Type Wave Energy Converter. J. Offshore Mech. Arct. Eng. 133, 041602–8. doi:10.1115/1.4003519

WAMIT, n.d. . WAMIT, Inc., Chestnut Hill, Massachusetts.

Wei, Y., Yang, J., Chen, G., Hu, Z., 2011. The Research of Moonpool Size Effect on the Hydrodynamic Performance of FDPSO, in: Proceedings of the ASME 2011 30th International Conference on Ocean, Offshore and Arctic Engineering. Presented at the International Conference on Ocean, Offshore and Arctic Engineering, Rotterdam, The Netherlands, pp. 459–467. doi:10.1115/OMAE2011-49586

Yang, S.-H., Kwon, S.-H., 2013. Experimental study on moonpool resonance of offshore floating structure. Int. J. Nav. Archit. Ocean Eng. 5, 313–323.